Materials & Design 206 (2021) 109795

Contents lists available at ScienceDirect

Materials & Design

journal homepage: www.elsevier.com/locate/matdes

Effect of processing parameters on the properties of freeze-cast Ni wick with gradient porosity

P.J. Lloreda-Jurado, E. Chicardi, A. Paúl, R. Sepúlveda *

Departamento de Ingeniería y Ciencia de los Materiales y del Transporte, E.T.S. de Ingenieros, Universidad de Sevilla, Avda. Camino de los Descubrimientos s/n., 41092 Sevilla, Spain

HIGHLIGHTS

- Gradient porous Ni wick have shown potential applications in LHP systems.
- NiO agglomerates were reduced to 33 nm in diameter using stearic acid in camphene.
- Stearic acid enhances stabilisation, dendrite replication, and pore connectivity.

GRAPHICAL ABSTRACT

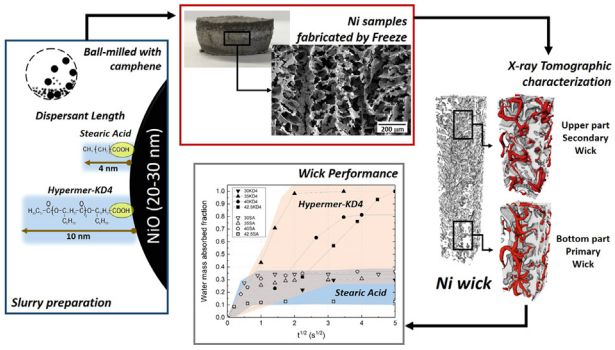

ARTICLE INFO

Article history:
Received 26 March 2021
Revised 17 April 2021
Accepted 2 May 2021
Available online 5 May 2021

Keywords:
Freeze-casting
Nickel
Wick
Camphene
Stearic acid
Nanoparticles

ABSTRACT

Wicks are the main component of Loop Heat Pipe systems, whereby coolant liquid flow through their porous structure. They are usually formed by a primary wick to produce liquid transportation by capillary force, and a secondary wick that is continuously wetted by the liquid coolant. Traditionally, the two wicks are manufactured separately and subsequently joined, thereby creating an interface that reduces the liquid transfer efficiency. In order to overcome this situation, a gradient porous wick is proposed and successfully manufactured through the freeze-casting method in a single operation. The influence of two different dispersant agents, KD4® and stearic acid was studied on the processing parameters, final pore size and morphology, and capillarity performances. A variate of gradient porosity was obtained by applying a diverse thermal gradient and solidification front velocity during directional solidification. The rheological characterisation of the camphene-based NiO suspensions was performed using a rotational viscometer. The final pore size and morphology were characterised by Optical Microscopy, Field Emission Scanning Electron Microscopy, and X-ray computed tomography. The use of stearic acid improves the particle stabilisation and generates pore enlargement with an equiaxed pore structure, while commercial dispersant KD4® shows a dendritic pore morphology at lower thermal gradient.

1. Introduction

Nowadays, loop heat pipes (LHP) play a major role in improving the performance of microelectronic devices [1,2], and spacecraft components [3]. An LHP system is an efficient heat-transfer device that works on a closed condensation-evaporation loop of a cooling fluid. Fig. 1 shows a schematic diagram of the LHP mechanisms, wherein the capillarity forces produced by a porous wick eliminate the need for any pumping equipment. Wicks are manufactured by means of loose sintering or cold-pressing with space holders and by using powdered materials such as nickel [4], titanium [5], and

* Corresponding author.
E-mail address: rsepulveda@us.es (R. Sepúlveda).

https://doi.org/10.1016/j.matdes.2021.109795

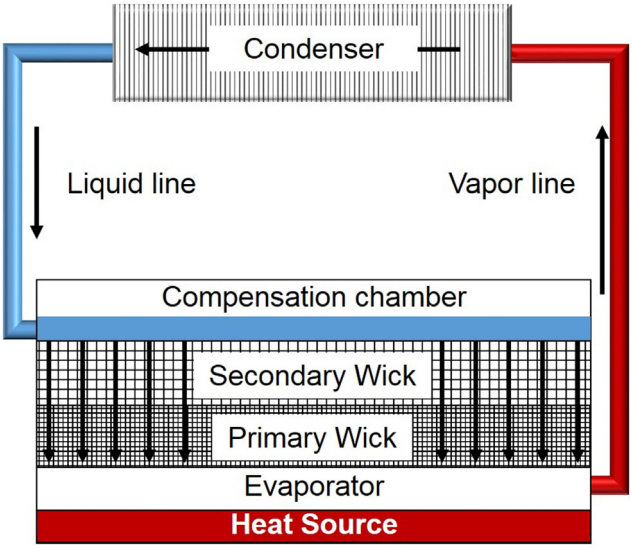

Fig. 1. Schema of a loop heat pipe. Wicks are porous structures having open pores of 1–100 μm in diameter with a porosity about of 50–75%.

stainless steel [6] due to their low-to-medium thermal conductivity, or copper [7] due to its high corrosion resistance. To ensure high heat-transfer capability during continuous operation, wicks should have high permeability and good capillarity with a low pressure drop. These features are obtained with an open pore structure with pore size and porosity ranges of 1–100 μm and 50–75%, respectively [8]. Additionally, sufficient mechanical strength (~10 MPa) must be guaranteed for dimensional tolerance adjustment, usually performed by electrical discharge machining. Since wicks need to be continuously wetted by the cooling fluid, a two-wick system is employed [4,9]. A primary wick with a smaller pore size ensures transportation of the liquid to the evaporator chamber, while a secondary wick with large pore size or of a different material connects the primary wick with the compensation chamber, thereby maintaining the condenser unit filled with the cooling fluid. Nevertheless, the two parts are manufactured separately and are subsequently joined, which creates an interface that could reduce the efficiency of the fluid transfer.

The efficiency of LHPs is linked to their ability to extract heat, which is reduced in electronic applications since wicks become thinner and smaller. To counterbalance this effect, materials of medium-range thermal conductivity are being tested with new designs of porous structures. In this respect, a new type of wick with a biporous capillary structure has been receiving much attention [10,11] due to its resulting increase in the heat-transfer coefficient in the evaporation zone. According to Maydanik et al. [8], this pore arrangement enables the effective evaporating layer of the wick to be increased, and the evaporator thermal resistance to be reduced by diminishing the average thickness of the walls.

For the development purposes of a new wick showing a gradient pore structure that eliminates the joining process, the Freeze-Casting (FC) technique could present a suitable and interesting option. Freeze-casting is a simple, low-cost and scalable method [12], which is appropriate for the creation of porous materials with tailored pore features, simply by altering the processing parameters [13,14]. This technique relies on the solidification of a liquid phase in which particles have been dispersed, since dendrites grow during solidification, the suspended particles are pushed and concentrated into the interdendritic spaces. The sublimation of the solidified phase creates a green body powder scaffold, which is then sintered at elevated temperature. The final porous structure can be adjusted through the selection of the raw powder material, the liquid medium [14], and the solidification rate. This technique has been extensively employed with submicronmetric ceramic powders using water [15] or camphene [16] as the dispersant media. Recently, the use of copper [17,18], nickel [19], and iron [20,21] oxide particles suspended in camphene has been successful in producing highly interconnected metallic porous structures, with wide pore-size distribution [22].

The use of nickel oxide particles through the FC process in water-based suspensions is widespread since it obtains porous materials for the application of solid oxide fuel cells (SOFCs) [23,24], while the use of camphene-based suspensions to produce Ni wicks remains limited. Nonetheless, recent research successfully developed Ni wicks by FC using a water-based suspension of metal particles [11]. The employment of camphene offers a wide range of benefits, such as anisotropic branched morphology with gradual pore sizes, large and elongated pores in the direction of solidification, and high percentages of interconnected porosity. Camphene also has a melting point above room temperature (42–44 °C) and it can be sublimated at ambient conditions, which reduces energy consumption during solidification and facilitates easier sublimation. However, its non-polar characteristic narrows the options for suitable additives. Therefore, most researchers have used polystyrene (PS) and anionic polyester oligomeric (commercially known as KD4® or Zeprhym®) as a binder and dispersant agent, respectively [16,25].

The main goal of this research involves the manufacture of a suitable Ni wick with interconnected gradient pore-size structure through FC technology, by employing NiO nanoparticles as the raw material. Furthermore, the influence of two dispersant agents, stearic acid and KD4, on the rheological behaviour of slurries is studied together with the final pore morphology and the capillary performance of Ni wicks. Finally, the pore-size gradient is correlated as a function of the cooling conditions applied.

2. Experimental procedures

2.1. Wick manufacturing.

Two different camphene (95% purity, Sigma Aldrich, Madrid, Spain) suspensions with 5 vol% of NiO nanoparticles (20–30 nm in diameter, GNM Oocap France SAS, St-Cannat, France) were created by adding 8 wt% of Hypermer™ KD4® (CRODA Ibérica SA, Barcelona, Spain) or stearic acid, SA, (98% purity, Alfa Aesar, Barcelona, Spain) as the dispersant agent. Each suspension was mixed by ball milling at 60 °C, where the dispersant was first incorporated into melted camphene and then mixed for 30 min. The NiO was then added and milled for 8 h. Finally, 20 vol% of PS (Mw = 350,000 g/mol, Sigma Aldrich, Madrid, Spain) was incorporated as the binder and mixed for an extra 3 h. The dispersant and binder doses were in accordance with the powder load.

After milling, the suspension was immediately poured into a cylindrical PTFE mould with a Cu base, preheated at 60 °C inside an incubator and pre-rested for 15 min before the solidification process started. An assisted solidification process, reported elsewhere [22], was initiated by running water at 30, 35, 40, or 42.5 °C through the mould base, and by reducing the incubator temperature by 0.2 °C/min. Green samples measured approximately 30 mm in diameter by 16 mm in height.

Sublimation of solid camphene within the samples was completed after 48 h in ambient conditions. Green samples underwent heat treatment at 600 °C for 2 h for organic burn-out in a N_2 gas flow (Airliquide, Seville, Spain), followed by a sintering process under reducing conditions at 1100 °C for 3 h with Ar-20H_2 gas flow (Airliquide, Seville, Spain). Through this step, NiO is reduced to form the resulting metallic nickel wicks. Heating and cooling rates

were set at 1 °C/min and 5 °C/min, respectively, to prevent cracks and sample distortions. Wick samples were denoted according to each cooling temperature and to the dispersant agent used: for example, 30SA corresponds to a sample solidified at 30 °C and using stearic acid as the dispersant agent.

2.2. Wick characterisation.

In order to determine the influence of the dispersant agent and the milling time on the suspension viscosity, a Myr VR 300 rotational viscometer with a low-viscosity adaptor (Viscotech Hispania S.L., Barcelona, Spain) was employed to measure the viscosity of each suspension at 4, 8, 12, and 24 h of milling times. Suspensions were first sonicated for 15 min and then kept inside the viscometer chamber for another 15 min to reduce the presence of air bubbles. All measurements were performed at 60 °C. At each milling time, the viscosity was determined by sequentially increasing the shear rate from 1.2 s^{-1} up to approximately 121.5 s^{-1}. Between measurements, an interval of 2 min was fixed to stabilise the dispersion system and prevent the formation of vortices due to the increasing shear rate. The viscosity values were kept constant regardless of whether they had been measured by increasing or decreasing the shear rate, and therefore no hysteresis loop was observed and the appearance of thixotropy or rheopexy effects could be considered negligible. One drop (approximately 0.05 ml) of each suspension was diluted in 10 ml liquid camphene to obtain the average particle diameter by Dynamic Light Scattering (DLS) technique using a Zetasizer Nano ZSP instrument (Malvern Instruments, Worcestershire, UK).

Two processing FC parameters, the solidification front velocity (V^h) and the average thermal gradient (G^h), were monitored by 4 thermocouples placed along the sample height (h) at 0, 4, 8, and 12 mm. V^h was calculated as the time that the suspension solidification temperature (T_{ss}) takes to move between thermocouples (4 mm), and G^h was defined as the temperature difference between sequential thermocouples at the moment that T_{ss} reached halfway. The following equations show the calculation procedure in greater detail.

$$V^{\mathrm{h}} = \frac{0.4\ cm}{t_{ss}^{\mathrm{h}} - t_{ss}^{\mathrm{h-4}}} \left[\frac{cm}{s}\right], (h = 4, 8, 12\ mm) \tag{1}$$

$$G^h = \frac{T_\tau^h - T_\tau^{h-4}}{0.4\,\mathrm{cm}} \left[\frac{^\circ\mathrm{C}}{\mathrm{cm}}\right] \text{ with } \tau = (t_{ss}^h - t_{ss}^{h-4})/2,\ (h = 4, 8, 12\,\mathrm{mm}) \tag{2}$$

where t_{ss}^{h} is the time to reach T_{ss} at h, and T_τ^{h} is the temperature measured at h at the time τ. T_{ss} was obtained by differential scanning calorimetry (DSC) analysis at 43.3 °C.

The average interconnected porosity was determined through Archimedes' method in accordance with the ASTM C373-18 standard, which involved soaking the wick samples in hot water for 24 h. Several Optical Microscopy (OM) and Field Emission Scanning Electron Microscopy (FESEM) images were taken on the central axial plane at different heights of each fabricated sample. The FESEM examination was performed with an accelerating voltage of 10 KV over the samples uncoated. These images were employed to estimate the average pore size and total porosity across the sample height by using the non-redundant maximum-sphere-fitted image analysis technique [26]. The pore morphology and interconnectivity of samples 30KD4 and 42.5KD4 were determined by X-ray computed tomography (X-CT) for comparison. X-CT measurements were carried out using a YXLON micro-tomograph (Hamburg, Germany) model Y.COUGAR-SMT on sub-samples (with an approximate volume of 1.2 mm × 1.2 mm × 2.5 mm) located in the lower and upper parts. The X-ray source operated at 60 KV and 8 μA to ensure a voxel size of 3 μm, the sub-samples were rotated over 360° to obtain 1440 projections during approximately 48 min of scan time. Subsequently, the Feldkamp cone-beam algorithm was used with each projection to reconstruct the 16-bit 2D cross-section images. The collected 2D cross-section images were pre-processed with ImageJ software (8-bit binarisation, threshold, and removal of 1-pixel outliers) and 3D visualisations were made using Avizo software.

In order to determine the capillary performance (i.e., the amount of liquid absorbed over time), samples were carefully placed in contact with the water reservoir, at room temperature (25 °C), by means of a micrometric screw. The weight of water absorbed over time was ascertained using an electronic scales. The top sample surface was placed in direct contact with the water to reproduce the effect of impregnation of the secondary wick and the capillarity suction towards the primary wick. Fig. 2 shows the experimental setup used in this work with details of the sample orientation (Fig. 2a) and the holding-movement system (Fig. 2b). Similar setups can be found in the literature that use water as the adsorbed liquid [27,28].

3. Results and discussion

3.1. Rheological behaviour of NiO camphene-based suspensions

Fig. 3a shows the influence of the two different dispersant agents, KD4® and SA, on the rheological behaviour of 5 vol% NiO camphene-based suspension over the milling time. These results illustrate the effect of the carbon-chain length when NiO nanoparticles are used. KD4 is a dispersant agent widely used in camphene suspensions prepared for freeze-casting, since it achieves suitable dispersion over submicron and micrometre particles. According to Moloney et al. [29], KD4 and SA employ their carboxyl functional group as a particle anchor. This functional group allows the formation of chelate complexes around the particle surfaces, keeping it strongly adsorbed to the particle while the other side of the molecule shows good affinity with the solvent. Both dispersants reduce the particle attraction forces through the steric barrier created by their carbon chains. The main difference between these two dispersants is the carbon-chain length of 10 and 4 nm for KD4 and SA, respectively. In the case of submicrometric particles [30], only KD4 is capable of achieving complete steric stabilisation, while SA could cover and isolate the particle successfully but its chain length is insufficient to achieve a complete steric stabilisation.

In the case of KD4®, Fig. 3a indicates that the rheological behaviour does not change significantly with the milling time. A calculated viscosity of 2.32 mPa·s was determined using a power-law model for a near-Newtonian fluid. This low viscosity value could be attributed to the low attractive energy existing between the particles due to the shielding effect produced by the long polymeric chain adsorbed. The long chains provide a thick layer of isolation, which reduces the electrical potential in the diffuse layer and results in a strong repulsion between particles due to the steric effect [31]. Therefore, this isolating thick layer inhibits the influence of the reduced mean particle size in the rheological behaviour of the tested milling times. As Fig. 3b shows a drastic reduction from 630 nm to 49 nm at 4 h and 24 h of milling time respectively.

When SA is used, the suspension exhibits rheological behaviour as a non-Newtonian fluid and the shear stress increases with the milling time, as can be deduced from Fig. 3a. Moreover, suspensions using SA show viscoelastic behaviour that can be fitted to a Herschel-Bulkley rheological model [32]. Table 1 shows the parameters obtained, such as yield point (τ_0), viscosity (η), and flow index (n) at various milling times. As the milling progresses, the yield

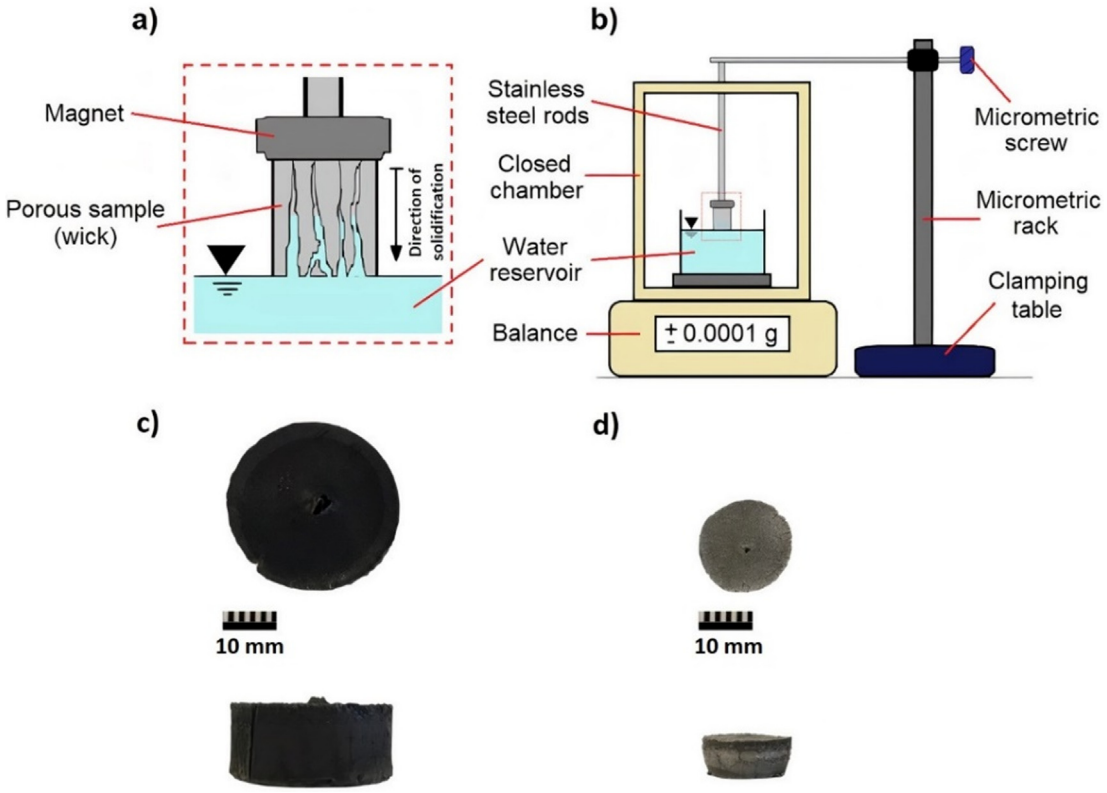

Fig. 2. Experimental setup employed to determine the capillary performance on the Ni wicks. Details of the sample orientation (a), the holding-movement system (b), NiO green sample (c), and Ni sintered sample (d) are shown. (For interpretation of the references to colour in this figure legend, the reader is referred to the web version of this article.)

point and the viscosity increase significantly and the flow index is reduced. The flow index ($n < 1$) obtained denotes shear-thinning behaviour of the NiO camphene-based suspension, this shear-thinning behaviour is an indication of weakly attractive, but non-touching, particle interaction. The increase in viscosity with the milling time could be also attributed to progressive reduction in particle size and the formation of a mono-disperse particle distribution (Fig. 3c), which is induced by the shear forces during the milling [33,34]. The mean particle size (by number %) went from 390 nm at 4 h of milling time to 33 nm and the end of the process. Therefore, the viscosity of the suspension increases as the influence of the smaller particle size become significant. The particle agglomerates in the suspension break up at new particle surfaces could be covered by a much thinner layer of SA. This weakly attractive interaction of smaller particles leads to a high-packing factor during aggregation throughout the process of solidification [34,35]. Therefore, SA constitutes a promising dispersant alternative in camphene-based suspensions of nanoparticles for its use in freeze-casting.

3.2. Microstructures of manufactured wicks

The differences in the particle interaction phenomena for each dispersant, previously verified by rheology characterisation, exert a major effect over the microstructure parameters of the wicks manufactured, such as the amount and type of porosity, the pore size, and its morphology. Fig. 4 shows the effect of the dispersant agent and the cooling temperature used on the calculated porosity across the sample height. KD4 creates a gradient porosity at all cooling temperatures, with the lowest porosity obtained in the lower part of the sample, while SA generates a practically constant value of porosity. Furthermore, the total porosity seems higher with the use of SA. This feature is more evident at the lower end since sample 30KD4 reaches 42% porosity and 30SA climbs up to 84% (Fig. 4). The porosity reduction in the lowest parts of those samples that use KD4 in their suspensions could be ascribed to particle sedimentation during the pre-resting and solidification steps.

This sedimentation modifies the particle concentration across sample height. As a consequence, the concentration in the liquid above the solidification front is continuously reduced as solidification progresses. This event results in a gradient total porosity, which varies from 42% at the lower part of the 30KD4 sample to 90% in the upper part of the 42.5KD4. Furthermore, the densification in the lower zone of samples dispersed with KD4 is promoted by the high concentration of particles and accentuated when the cooling temperature employed is lower (i.e., when the solidification front velocity (V^h) and the average thermal gradient (G^h) are higher), and increases from 42%, in samples 30KD4 (cooled at 30 °C), up to 63% in samples 42.5KD4 (cooled slowly at 42.5 °C). Particle sedimentation could be attributed to the formation of heavier particles due to various factors, such as particle agglomerates not fully dispersed during the milling process, as shows Fig. 3b with a mean particle size (by number) of 49 nm, the higher molecular weight of KD4 (1414.3 g/mol) attributed to its long carbon chains, and a certain level of entanglement occurring between the PS and camphene molecules [29]. Likewise, this effective enlargement of the particle size decreases the critical velocity for particle engulfment (V_{cr}) [36]; at lower V^h, particles will be surrounded by the growing camphene crystal during solidification, instead of being pushed into the interdendritic spaces. Therefore, a pore morphology with smaller pore size could be produced.

Related to the samples dispersed with SA, the sedimentation behaviour is lessened. The porosity values reported are around 90 vol% across the sample height. Therefore, these suspensions

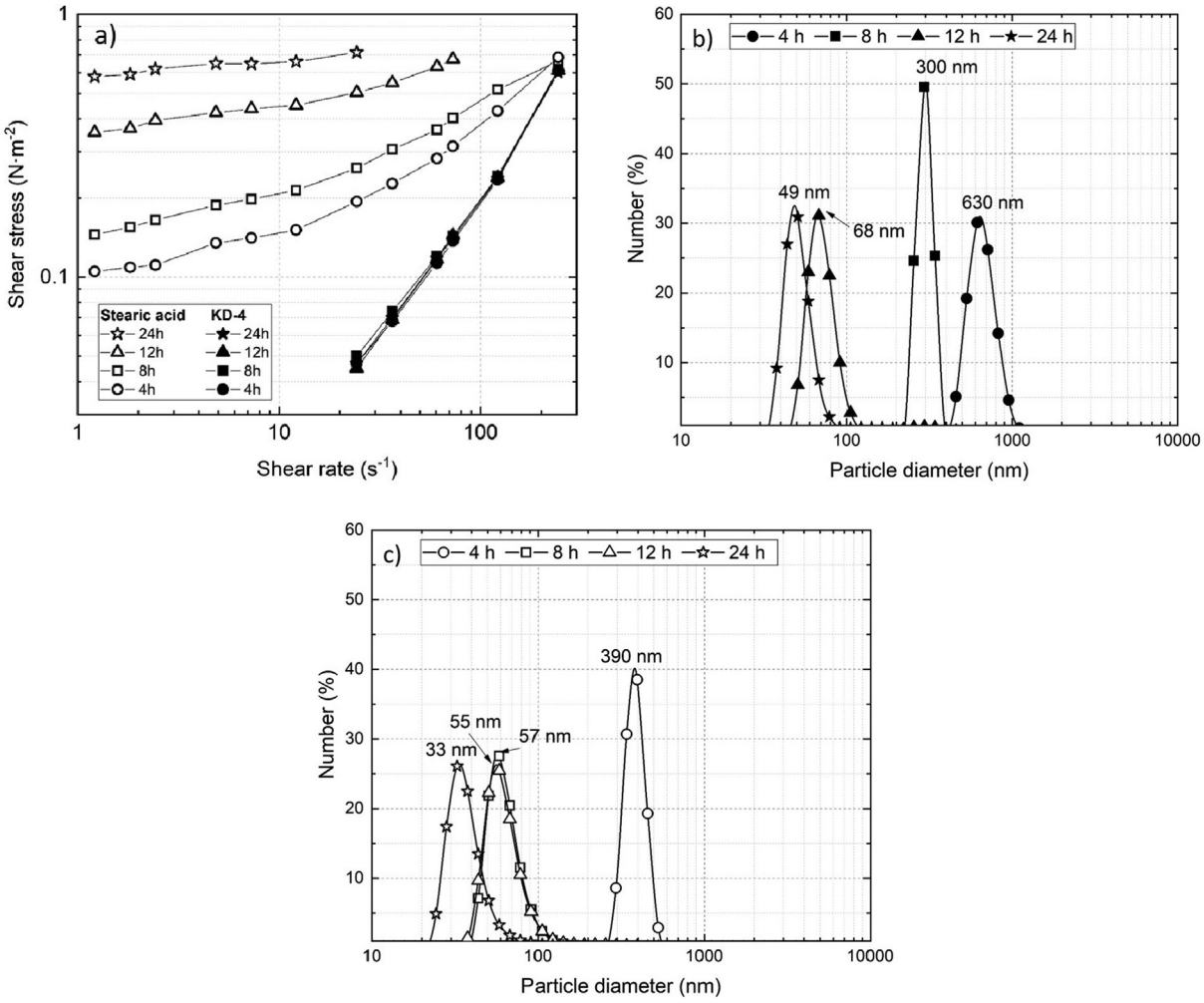

Fig. 3. Influence of the dispersant agents on the rheological behaviour (a) and the particle diameter (b,c) of 5 vol% NiO camphene-based suspensions over the milling time (4, 8, 12, and 24 h). KD4® is in solid marks and SA in hollow marks.

Table 1
Herschel-Bulkley model parameters at different milling times.

Herschel-Bulkley model: $\tau = \tau_0 + \eta \dot{A} \cdot \gamma^n$			
Milling time (h)	τ_0 (N·m^{-2})	η (mPa·s)	n
4	0.10	6	0.83
8	0.13	17	0.64
12	0.34	27	0.58
24	0.58	27	0.54

seem more stable despite not generating a complete steric effect as compared with KD4. The nanometric particles of NiO used in this research show a higher degree of dispersion in a non-polar media (camphene) when a short carbon-chain additive (SA) is employed. Stearic acid seems to reduce the weight and effective size of the particles down to 33 nm (Fig. 3c), which allows an increase in V_{cr} that enables particle pushing and redistribution during the camphene solidification. Furthermore, SA reduced the tendency to form agglomerates or molecule entanglements with PS or the solvent.

In samples with SA, the interconnected porosity obtained by Archimedes' method (Fig. 4) was lower than the total porosity, meaning that close porosity was well-distributed across the sample height and properly detected by the measurement technique. In contrast, in the sample with KD4, the interconnected porosity

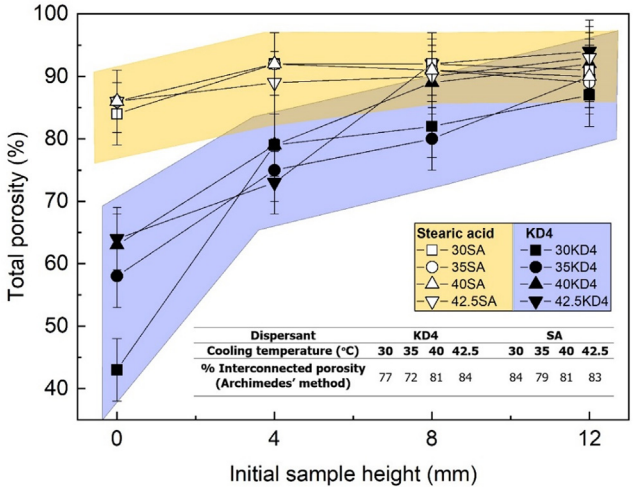

Fig. 4. Influence of the dispersant agent and the cooling temperature on the total porosity of the Ni wick across the sample height. Total sample porosity was calculated using image analysis over the optical microscopy images taken at the corresponding initial sample height. The table inserted shows the interconnected porosity obtained by the Archimedes method.

was preferentially located from the middle to the top part of the sample, thereby showing the tendency of particle sedimentation effect in the samples with KD4.

According to Fig. 5, a significant pore morphology modification across the sample height is observed when the cooling temperature and dispersant agent varies. The KD4 dispersant generates a greater pore size and morphology variation along with sample height than SA. Notably, the pore structure created during the directional solidification retains its many features after the thermal cycle of reduce-sintering. The variation in porosity along with height is promoted by the application of the directional solidification during the sample fabrication. The creation of a gradient pore-size structure is now visible, where fewer and smaller pores can be observed in the lower part of the samples, and pore size is then increased as the cooling rate diminishes. The gradient porosity is enhanced in samples with KD4 due to the particle sedimentation, especially at the sample 30KD4 (Fig. 5). The number of small pores in the lower part of the sample is moderated as the cooling temperature increases.

The use of SA leads to larger pore sizes with less variation (gradient) according to the sample height. NiO powder dispersed with SA in camphene-based suspensions shows smaller effective particle size, as is demonstrated by the increase of viscosity with the milling time (Fig. 3), and the particle concentration remains constant during solidification. While V^h increases and G^h decreases, the smaller NiO particles are pushed much further since the camphene crystal interface experiences a transition from cellular to equiaxed [37]. The dendrite contour is also more recognisable since the particle stacking and formation of the secondary arms have been promoted. Ultimately, larger pores have fewer probabilities to disappear during the reduction-sintering heat treatment. It should be emphasised that, after the sintering process under reducing conditions, the pore structure created during directional solidification retains its many features.

Cooling conditions show a clear influence not only on the pore size, but also on the pore morphology. Once the solidification starts, dendrite growth is driven by the high G^h and low V^h leading to an elongated crystal. During the course of solidification, G^h is reduced and V^h increased, and camphene dendrite turns gradually in to an equiaxed crystal since secondary and tertiary arms can grow more easily due to mitigation of the directional cooling and the lower possibility of particle entrapment [22]. This change in pore morphology is visible in Fig. 5 and is correlated as a function of G^h and V^h in Fig. 6. Fig. 6 also shows the increment in the final pore size of the fabricated Ni wicks as a function of the cooling temperature (30, 35, 40, and 42.5 °C) and the initial sample height (h = 4, 8, and 12 mm), whereby both dispersants reveal a strong dependency of G^h and V^h on pore size and morphology obtained during the FC. Nevertheless, under similar cooling conditions, SA produced wider, more equiaxed pores.

Fig. 7 shows the 3D reconstruction of the Ni wicks 30KD4 and 42.5KD4 in their lowest and topmost parts, respectively. In the lower part of sample 30KD4 (Fig. 7a-b) with the highest G^h and the lowest V^hrecorded, this cooling condition produced a highly interconnected structure of narrow porous channels aligned with the direction of the solidification, as can be seen in the pore skeleton render (Supplementary Material, Fig. 7Sa-Sb). On the other hand, in the upper part of the sample 42.5KD4 (Fig. 7c-d), which showed the lowest G^h and the highest V^h, a broadening of the pore size, and a transition from a dendritic and branched morphology to a more equiaxed morphology occurred due to the reduction of the number of pore connections (Supplementary Material, Fig. 7Sc-Sd). Indeed, as the solidification front moves through the sample, the

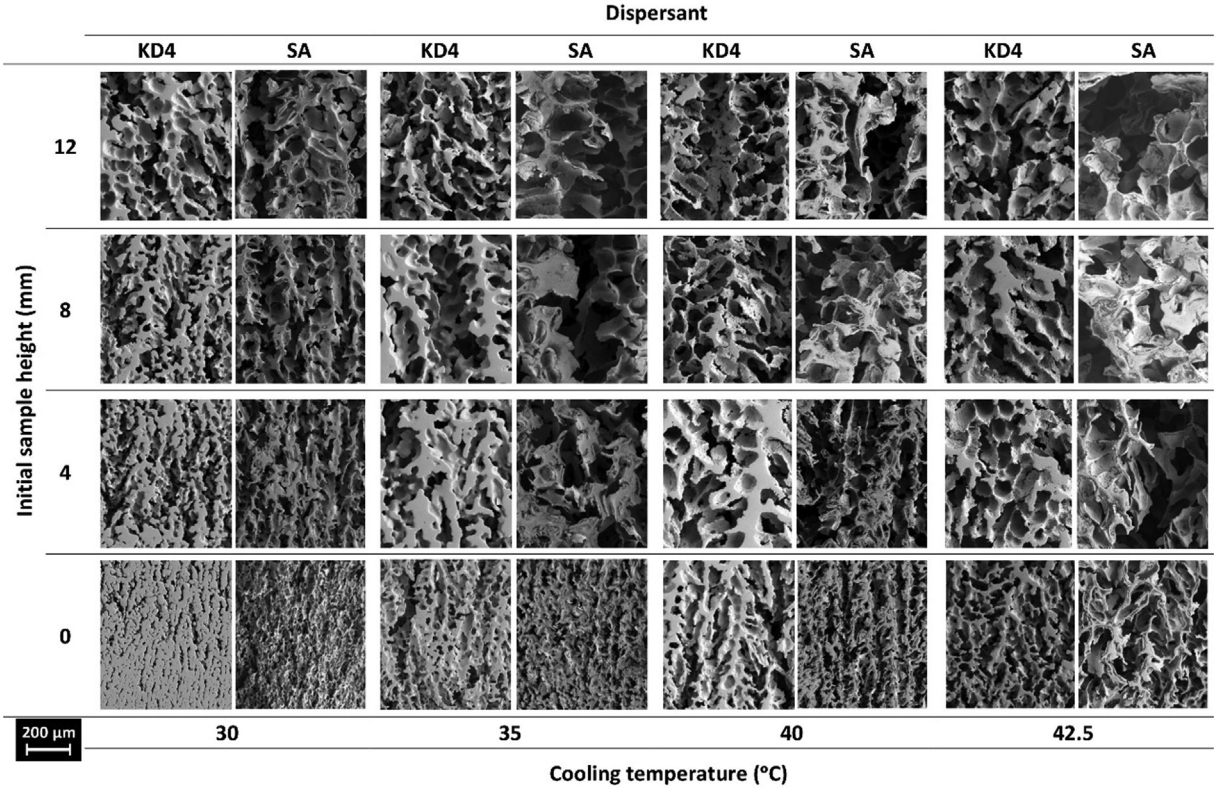

Fig. 5. Effect of cooling temperatures (30, 35, 40, and 42.5 °C) and the dispersant agent (KD4 or SA) on the pore morphology of Ni wicks across the initial sample height.

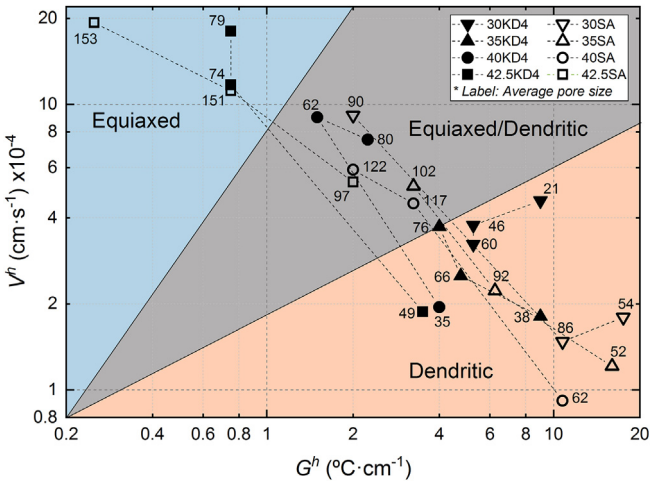

Fig. 6. Average pore size and typical morphology features of the Ni wicks as a function of the average thermal gradient (Gh) and solidification front velocity (Vh) measured at different heights(h = 4, 8, and 12 mm) during sample solidification. Point labels indicate the average pore size in microns obtained at each cooling temperature (30, 35, 40, and 42.5 °C) and dispersant employed (KD4 or SA). Equiaxed and dendritic refers to its characteristic microstructure.

directional driving force of the solidification diminishes due to the continuous reduction of G^h, as shown in Fig. 6.

3.3. Capillary performance of fabricated wicks

Fig. 8 shows the fraction of water mass absorbed due to the interconnected porosity versus time as a function of the dispersant and cooling temperature. A value of 1 indicates that all open pores were filled with water during the capillary test. Ni wicks manufactured with KD4 have shown a higher mass absorption than those with SA. They have presented a large-pore alignment (i.e., dendritic pore morphology is widely extended) with the direction of solidification parallel to the advancing liquid front. Sample 30KD4 (Fig. 8) presents the lowest adsorption rate and failed to did not completely fill despite having a wide dendritic pore morphology and the smallest pore size. This behaviour could be attributed to the lack of interconnected porosity (Fig. 4) produced by the particle sedimentation at the bottom of the wick (Fig. 5). Samples 42.5, 40, and 35KD4 present an increased absorption rate, respectively, as they show a lower extent of the equiaxed pore morphology in their top sections (Fig. 6). Wicks made from suspensions dispersed with SA (30–42.5SA) have similar absorption rates (Fig. 8), and reach a maximum fraction of absorbed water mass of 0.35, due to their similar pore sizes and widely extended equiaxed pore morphology through the sample (Fig. 6). This behaviour is enhanced on the 42.5SA sample, which, despite possessing the largest pore size, shows the lowest absorption rate due to its completely equiaxed pore structure (Fig. 6).

The Lucas-Washburn's (LW) law [38] (Eq. (3)), it has been successfully applied to model and characterise the capillary pumping performance [27,28] of wick samples according to the absorbed fluid mass (m):

$$m = \frac{\delta \cdot P \cdot S}{2} \cdot \left(\frac{\sigma \cdot \varnothing}{\mu}\right)^{1/2} \cdot (t)^{1/2} \quad (3)$$

where δ is the fluid (water) density, P is the interconnected porosity (obtained by Archimedes' method), S is sample surface in contact with the fluid, σ is the surface tension, $\varnothing$ is the pore size, μ is the dynamic viscosity, and t is the time. The LW law describes the capillary flow in a straight pore as a function of time, therefore the fraction of water mass absorbed by the open pores was used in Fig. 8. Despite its limitation, the behaviour predicted for porous materials fits to those with pores are oriented perpendicular to the fluid surface and that resemble straight cylinders, although several modifications, such as gravity, fluid evaporation, tortuosity, and pore shape, have been proposed for it to adequately fit a broad range of situations. In the case of Ni wicks fabricated by the FC technique, the absorption rates fall under the predicted values of LW law for a porous sample with a 80% of open porosity and pore size ($\varnothing$) of 5 or

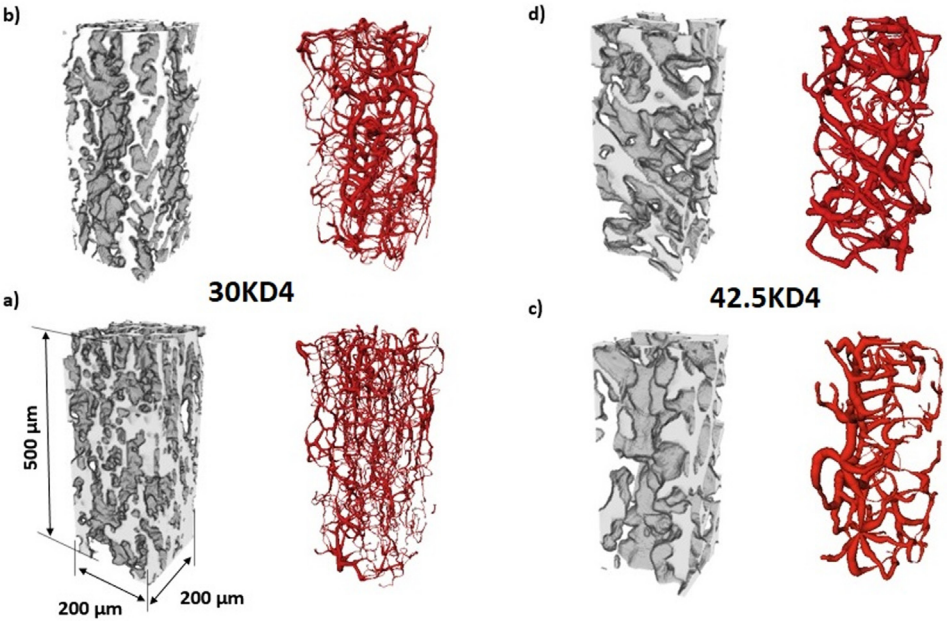

Fig. 7. 3D reconstructions from X-ray computed tomography (X-CT) of Ni wicks fabricated by freeze-casting using KD4 dispersant at two cooling conditions 30 °C (a–b) and 42. 5 °C (c–d). Samples (grey) and pore skeleton (red) were rendered at different initial sample heights: 0 (a), 4 mm (b) for sample 30KD4, 8 (c), and 12 (d) mm for sample 42.5KD4. All reconstructed parallelepipeds are approximately 200 × 200 × 500 µm in size. Supplementary material (Fig. 7Sa-d) shows the 3D reconstructions rotating and morphing to the pore skeleton representation. (For interpretation of the references to colour in this figure legend, the reader is referred to the web version of this article.)

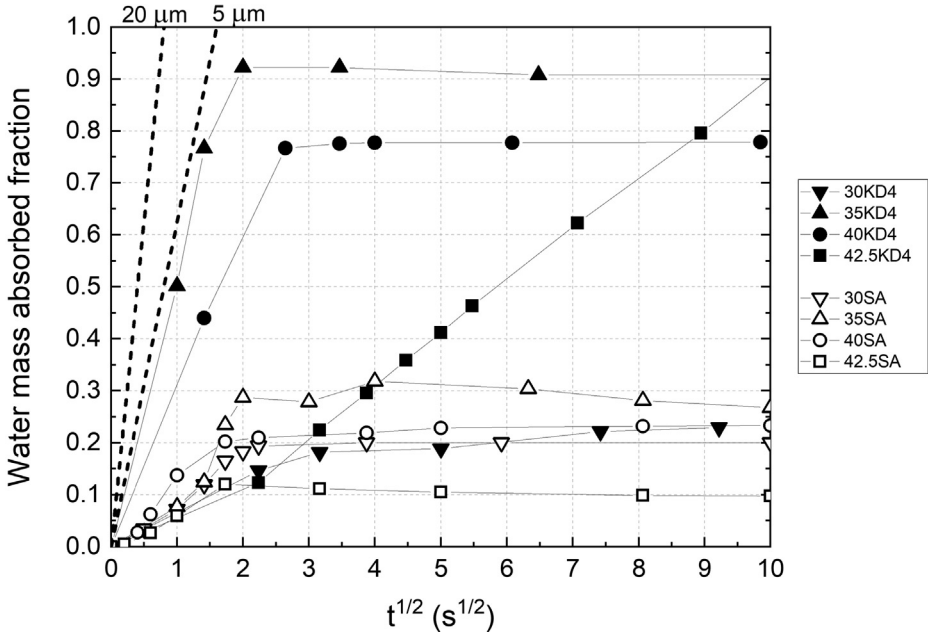

Fig. 8. Water mass absorbed fraction over time of the Ni wicks as a function of the dispersant agent (KD4 or SA) and the cooling temperature (30, 35, 40, and 42.5 °C). Dotted lines are predicted values by the LW law for a porous sample with a 80% of open porosity and pore size (∅) of 5 and 20 µm.

20 µm (dotted lines in Fig. 8), most likely due to the influence of the pore morphology.

A fractal dimension for the tortuosity factor (D_T) has recently been proposed [39] [50] as $t^{1/2D_T}$ in a derivation of the LW law (e.g., LW law applied with $D_T = 1$), in order to consider the variety of pore shapes and interconnectivity levels. This factor has already been employed to correct the influence of the pore morphology in samples fabricated by FC [40], and validates the influence of dendritic pore morphology in the improvement of the ability of liquid to flow through a porous structure.

4. Conclusions

Ni wicks with gradient porosity were successfully fabricated by the freeze-casting technique. The processing modification implemented confirmed the effect of the dispersant agent on the final microstructure and on the wick performance. Stearic acid has been demonstrated to improve microstructural characteristics, such as dendrite contour definition (i.e., high tortuosity), and to increase the pore size. The use of dispersant with a short carbon-chain length creates a suspension of greater stability, reduces particle sedimentation thereby preserving the pouring ability. However, when stearic acid is employed, the applied thermal gradient must be incremented to ensure a more directional dendritic pore structure, which constitutes the key factor for improved wick performance. In this regard, although KD4 shows higher particle sedimentation, it was able to promote (within the cooling rate employed) a more dendritic pore structure across the wick height.

The wick performance is linked to the dendritic pore size and the extension of the primary arm. Here, the stearic acid as dispersant agent in camphene-based suspensions of nanoparticles for freeze-casting was use for the first time, to the best of our knowledge. This promising dispersant alternative creates low viscosity slurries, diminishes the particle sedimentation and enhances pore interconnectivity, although higher thermal gradients must be applied in order to increment the number of elongated camphene dendrites during solidification for the capillarity performance to be improved

Declaration of Competing Interest

The authors declare that they have no known competing financial interests or personal relationships that could have appeared to influence the work reported in this paper.

Acknowledgements

Financial support for this work has been provided by the Ministerio de Ciencia e Innovación – Agencia Estatal de Investigación through the project MAT2016-76713-P co-funded by European Regional Development Fund. Lloreda-Jurado P.J. also thanks to the Universidad de Sevilla for the financial support (grant PIF II.2A, through VI Plan Propio de Investigación).

Data availability

The raw data required to reproduce these findings are available to download from http://www.inciemat.es/. The processed data required to reproduce these findings are available to download from http://www.inciemat.es/.

Appendix A. Supplementary material

Supplementary data to this article can be found online at https://doi.org/10.1016/j.matdes.2021.109795.

References

[1] H. Tang, Y. Tang, Z. Wan, J. Li, W. Yuan, L. Lu, Y. Li, K. Tang, Review of applications and developments of ultra-thin micro heat pipes for electronic cooling, Appl. Energy. 223 (2018) 383–400, https://doi.org/10.1016/j.apenergy.2018.04.072.

[2] A.B. Solomon, A.K. Mahto, R.C. Joy, A.A. Rajan, D.A. Jayprakash, A. Dixit, A. Sahay, Application of bio-wick in compact loop heat pipe, Appl. Therm. Eng. 169 (2020), https://doi.org/10.1016/j.applthermaleng.2020.114927 114927.

[3] H. Cho, L. Jin, S. Jeong, Experimental investigation on performances and characteristics of nitrogen-charged cryogenic loop heat pipe with wick-mounted condenser, Cryogenics (Guildf). 105 (2020), https://doi.org/10.1016/j.cryogenics.2019.08.001 102970.

[4] W. Tian, S. He, Z. Liu, W. Liu, Experimental investigation of a miniature loop heat pipe with eccentric evaporator for cooling electronics, Appl. Therm. Eng. 159 (2019), https://doi.org/10.1016/j.applthermaleng.2019.113982 113982.
[5] N.S. Ramasamy, P. Kumar, B. Wangaskar, S. Khandekar, Y.F. Maydanik, Miniature ammonia loop heat pipe for terrestrial applications: Experiments and modeling, Int. J. Therm. Sci. 124 (2018) 263–278, https://doi.org/10.1016/J.IJTHERMALSCI.2017.10.018.
[6] S. Zhang, C. Chen, G. Chen, Y. Sun, Y. Tang, Z. Wang, Capillary performance characterization of porous sintered stainless steel powder wicks for stainless steel heat pipes, Int. Commun. Heat Mass Transf. 116 (2020), https://doi.org/10.1016/j.icheatmasstransfer.2020.104702 104702.
[7] Z. Wan, J. Deng, B. Li, Y. Xu, X. Wang, Y. Tang, Thermal performance of a miniature loop heat pipe using water–copper nanofluid, Appl. Therm. Eng. 78 (2015) 712–719, https://doi.org/10.1016/j.applthermaleng.2014.11.010.
[8] Y.F. Maydanik, M.A. Chernysheva, V.G. Pastukhov, Review: Loop heat pipes with flat evaporators, Appl. Therm. Eng. 67 (2014) 294–307, https://doi.org/10.1016/j.applthermaleng.2014.03.041.
[9] A. Joseph Mathews, S. Ranjan, A. Inbaoli, C.S. Sujith Kumar, S. Jayaraj, Optimization of the sintering parameters of a biporous copper-nickel composite wick for loop heat pipes, Mater. Today Proc. (2020), https://doi.org/10.1016/j.matpr.2020.02.171.
[10] S. Sudhakar, J.A. Weibel, S.V. Garimella, Experimental investigation of boiling regimes in a capillary-fed two-layer evaporator wick, Int. J. Heat Mass Transf. 135 (2019) 1335–1345, https://doi.org/10.1016/j.ijheatmasstransfer.2019.03.008.
[11] T. Lin, T. Gan, X. Quan, P. Cheng, Fabricating metal wicks by LMC-like continuous directional freeze casting, J. Mater. Process. Technol. 282 (2020), https://doi.org/10.1016/j.jmatprotec.2020.116641 116641.
[12] K. Araki, J.W.J.W. Halloran, New freeze-casting technique for ceramics with sublimable vehicles, J. Am. Ceram. Soc. 87 (2004) 1859–1863, https://doi.org/10.1111/j.1151-2916.2004.tb06331.x.
[13] S. Deville, Ice-templating, freeze casting: Beyond materials processing, J. Mater. Res. 28 (2013) 2202–2219, https://doi.org/10.1557/jmr.2013.105.
[14] W.L. Li, K. Lu, J.Y. Walz, Freeze casting of porous materials: review of critical factors in microstructure evolution, Int. Mater. Rev. 57 (2012) 37–60, https://doi.org/10.1179/1743280411Y.0000000011.
[15] T.A. Ogden, M. Prisbrey, I. Nelson, B. Raeymaekers, S.E. Naleway, Ultrasound freeze casting: fabricating bioinspired porous scaffolds through combining freeze casting and ultrasound directed self-assembly, Mater. Des. 164 (2019), https://doi.org/10.1016/j.matdes.2018.107561 107561.
[16] H. Lee, H.-D. Jung, M.-H. Kang, J. Song, H.-E. Kim, T.-S. Jang, Effect of HF/HNO3-treatment on the porous structure and cell penetrability of titanium (Ti) scaffold, Mater. Des. 145 (2018) 65–73, https://doi.org/10.1016/j.matdes.2018.02.059.
[17] A.I.C. Ramos, D.C. Dunand, Preparation and characterization of directionally freeze-cast copper foams, Metals (Basel). 2 (2012) 265–273, https://doi.org/10.3390/met2030265.
[18] S.T. Oh, S.Y. Chang, M.J. Suk, Microstructure of porous Cu fabricated by freeze-drying process of CuO/camphene slurry, Trans. Nonferrous Met. Soc. China (English Ed. 22 (2012) s688–s691, https://doi.org/10.1016/S1003-6326(12)61787-7.
[19] Y.-H. Koh, J.-J. Sun, H.-E. Kim, Freeze casting of porous Ni–YSZ cermets, Mater. Lett. 61 (2007) 1283–1287, https://doi.org/10.1016/j.matlet.2006.07.009.
[20] R. Sepúlveda, A.A. Plunk, D.C. Dunand, Microstructure of Fe2O3 scaffolds created by freeze-casting and sintering, Mater. Lett. 142 (2015) 56–59, https://doi.org/10.1016/j.matlet.2014.11.155.
[21] T. Um, S.K. Wilke, H. Choe, D.C. Dunand, Effects of pore morphology on the cyclical oxidation/reduction of iron foams created via camphene-based freeze casting, J. Alloys Compd. (2020), https://doi.org/10.1016/j.jallcom.2020.156278 156278.
[22] P.J. Lloreda-Jurado, E.M. Pérez-Soriano, A. Paúl, J. Herguido, J.A. Peña, R. Sepúlveda, Doped iron oxide scaffolds with gradient porosity fabricated by freeze casting: pore morphology prediction and processing parameters, Mater. Sci. Technol. 36 (2020) 1227–1237, https://doi.org/10.1080/02670836.2020.1765096.
[23] Y. Chen, J. Bunch, T. Li, Z. Mao, F. Chen, Novel functionally graded acicular electrode for solid oxide cells fabricated by the freeze-tape-casting process, J. Power Sources. 213 (2012) 93–99, https://doi.org/10.1016/j.jpowsour.2012.03.109.
[24] S. Lee, J. Tam, W. Li, B. Yu, H.J. Cho, J. Samei, D.S. Wilkinson, H. Choe, U. Erb, Multi-scale morphological characterization of Ni foams with directional pores, Mater. Charact. 158 (2019), https://doi.org/10.1016/j.matchar.2019.109939 109939.
[25] S.H. Park, S.-M. Park, S.-J. Park, B.-Y. Park, S.-T. Oh, Porous W-Ni alloys synthesized from camphene/WO3-NiO slurry by freeze drying and heat treatment in hydrogen atmosphere, Korean J. Mater. Res. 28 (2018) 108–112, https://doi.org/10.3740/MRSK.2018.28.2.108.
[26] T. Hildebrand, P. Rüegsegger, A new method for the model-independent assessment of thickness in three-dimensional images, J. Microsc. 185 (1997) 67–75, https://doi.org/10.1046/j.1365-2818.1997.1340694.x.
[27] D. Wang, X. Wang, P. Zhou, Z. Wu, B. Duan, C. Wang, Influence of packing density on performance of porous wick for LHP, Powder Technol. 258 (2014) 6–10, https://doi.org/10.1016/j.powtec.2014.03.004.
[28] Y. Grebenyuk, H.X. Zhang, M. Wilhelm, K. Rezwan, M.E. Dreyer, Wicking into porous polymer-derived ceramic monoliths fabricated by freeze-casting, J. Eur. Ceram. Soc. 37 (2017) 1993–2000, https://doi.org/10.1016/j.jeurceramsoc.2016.11.049.
[29] V.M.B. Moloney, D. Parris, M.J. Edirisinghe, Rheology of zirconia suspensions in a nonpolar organic medium, J. Am. Ceram. Soc. 78 (1995) 3225–3232, https://doi.org/10.1111/j.1151-2916.1995.tb07958.x.
[30] S. Zürcher, T. Graule, Influence of dispersant structure on the rheological properties of highly-concentrated zirconia dispersions, 25 (2005) 863–873. doi: 10.1016/j.jeurceramsoc.2004.05.002.
[31] J.A. Lewis, Colloidal processing of ceramics, J. Am. Ceram. Soc. 83 (2004) 2341–2359, https://doi.org/10.1111/j.1151-2916.2000.tb01560.x.
[32] W.H. Herschel, R. Bulkley, Konsistenzmessungen von Gummi-Benzollösungen, Kolloid-Zeitschrift. 39 (1926) 291–300, https://doi.org/10.1007/BF01432034.
[33] S. Pednekar, J. Chun, J.F. Morris, Bidisperse and polydisperse suspension rheology at large solid fraction, J. Rheol. (N. Y. N. Y). 62 (2018). 513–526. doi:10.1122/1.5011353.
[34] S. Olhero, J.M. Ferreira, Influence of particle size distribution on rheology and particle packing of silica-based suspensions, Powder Technol. 139 (2004) 69–75, https://doi.org/10.1016/j.powtec.2003.10.004.
[35] J.-H.J.-H. Lee, T.-Y.T.-Y. Yang, S.-Y.Y. and H.-C. Park*, S.-Y. Yoon, H.-C. Park, Suspension characteristics and rheological properties of TBA-based freeze casting alumina/zirconia slurries, JCPR. 013 (2012) 23–27. doi:10.36410/jcpr.2012.13.1.23.
[36] S. Sen, W.F. Kaukler, P. Curreri, D.M. Stefanescu, Dynamics of solid/liquid interface shape evolution near an insoluble particle - an X-ray transmission microscopy investigation, Metall. Mater. Trans. A Phys. Metall. Mater. Sci. 28 (1997) 2129–2135, https://doi.org/10.1007/s11661-997-0170-y.
[37] R. Trivedi, W. Kurz, Metals Handbook, Ninth Edit, 1988.
[38] E.W. Washburn, The dynamics of capillary flow, Phys. Rev. 17 (1921) 273–283, https://doi.org/10.1103/PhysRev.17.273.
[39] J. Cai, B. Yu, A discussion of the effect of tortuosity on the capillary imbibition in porous media, Transp. Porous Media. 89 (2011) 251–263, https://doi.org/10.1007/s11242-011-9767-0.
[40] D. Schumacher, D. Zimnik, M. Wilhelm, M. Dreyer, K. Rezwan, Solution based freeze cast polymer derived ceramics for isothermal wicking - relationship between pore structure and imbibition, Sci. Technol. Adv. Mater. 20 (2019) 1207–1221, https://doi.org/10.1080/14686996.2019.1699766.